Romanian Academy Cluj-Napoca Branch

Astronomical Observatory Cluj-Napoca

Executive Summary Report

Magnetic field perturbations by thermo-electric effects

Project Acronym	TherMag
Project Title	Magnetic field perturbations by thermo-electric effects
Contract Number	4000122501/17/NL/LvM/md
Project Coordinator	Romanian Academy, Cluj-Napoca Branch, Astronomical Institute
Project Manager	Gabriela Raluca Blaga gabriela.mocanu@academia-cj.ro +40743810625
Kick Off Date	18 January 2018
Contract Duration	12 months
ESA Technical Officer	Bálint Szücs Balint.Szucs@esa.int

January 2019

Document change log

Issue	Issue Date	Page Affected	Remarks	Initiator
2	11-02-2019	4	The 'I' is generally (at least in the electric engineering world) the sign for electric current, and as the direction of the current is by definition opposite to the movement of the electrons, it might be good to clarify if the 'Ithermal' is meant to be a current or electron flow. If it is electron flow, maybe the use of 'e' instead of 'I' would be better.	BS (TO)
			Reply: We modified the notation in Figure 1.1, from Ithermal to e-thermal motion and from Ielectric to e-electric motion. The text accompanying this Figure is also changed accordingly.	
2	11-02-2019	9	Figure 2.1 - Same comment as the previous, the direction of currents can be misleading, please check.	BS (TO)
			Reply: Indeed, the figure is drawn for the real motion of electrons. We have replaced I with j (current density) in the Figure and modified the text accordingly.	
2	11-02-2019	10	Figure 2.2 MLI - I couldn't find the definition of the abbreviation in the document, please define on first use. (MLI - Multi-Layer Insulation)	BS (TO)
			Reply: Modified accordingly	

Chapter 1

Scope and context

Moving charges produce magnetic fields. Since thermal transients produce an electric current, thermal transients produce magnetic fields. It has been shown that generation of these magnetic fields in the vicinity of sensitive instruments leads to a degradation of recorded data [1], [2], [3].

Getting closer to a theoretical solution and to an effective mitigation technique will help magnetic missions in ESA's Science Programme, Earth Observation Programme and, in fact, all missions that employ magnetic-sensitive sensors. The four objectives stated below contain a step-by-step approach to achieving this goal, as per [1], [4]:

(O_1) Identify physical processes involved in generation of thermoelectric and thermomagnetic currents;

(O_2) Formulate complete set of equations to describe dynamic thermoelectric and thermomagnetic effects;

(O_3) Predict numerical values for vector magnetic field generated by thermoelectric and thermomagnetic currents for a space mission and compare with available measurement data of materials used on board of spacecrafts;

(O_4) Identify main contributors to the effect and propose mitigation.

This work applies to systems where electric current and heat flow occur simultaneously. The resulting effects are classified with respect to the existence of an external magnetic field as:

- *thermoelectric effects*: simultaneous electric current and heat flow with a zero external magnetic field,
- *thermomagnetic effects*: simultaneous electric current and heat flow when a non-zero external magnetic field is present.

Historically, "thermomagnetic effect" is the name given to the group of effects generated by the influence of an external magnetic field on the electric and thermal properties of conductors and semiconductors subjected to a temperature gradient [5]. Such effects are documented both theoretically and experimentally in existing literature.

This project was set out to analyze the partially overlapping following problem $\mathcal{P}$: A metal (conductor) is subjected to a temperature gradient ∇T. Due to this gradient, electrons circulate and, in some cases, a current loop is set up. This current loop produces a magnetic field. This is the magnetic field we were interested in.

The literature offers only a a handful of references regarding the problem $\mathcal{P}$, mainly in [6] (here the author refers to the problem as the **new thermomagnetic effect**), and in the literature stemming from the SWARM[1] data analysis, e.g. [2].

The problem $\mathcal{P}$ was divided into four processes[2]:

1. A temperature gradient causes electron motion, as observed experimentally and shown concisely in linear nonequilibrium thermodynamics;

[1] For details on the SWARM mission, please see [13].

[2] What causes the actual temperature gradient is an external cause and not of interest here.

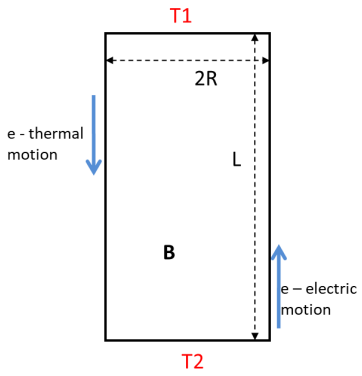

Figure 1.1: Schematic representation of how a coherent electron current loop is set up as a consequence of a thermal gradient.

2. The moving electrons interact with their environment and they scatter by phonons; in the temperature range of interest, thermal and electrical conductivities are limited by these collisions and may be calculated based on quantum mechanical models;

3. The thermally activated electrons (e-thermal motion) lead to a displacement of charge, which creates up a field $\vec{E}$. In turn, this field leads to the formation of an electric current (e-electric motion). As a consequence a (coherent) electron loop appears, of calculable intensity;

4. The electron current generates a magnetic field vector of calculable intensity and direction (Figure 1.1).

Embedding the already existing bits and pieces of empirical laws, theoretical derivations and observational data increases the chances to build a framework for solving the problem $\mathcal{P}$. As such, a body of knowledge was needed concerning:

- three sets of parameters:
  - material parameters (e.g., mass density of the metal)
  - parameters external to the material (e.g., temperature, external magnetic field)
  - fundamental constants (e.g., Boltzmann constant, magnetic permeability in vacuum)
- laws governing the physical processes;
- parameters specific to the physical configuration (e.g., geometry);

Tables with numerical values for these parameters were compiled from various sources where existent of calculated based on existing theoretical formulas.

With the aim of describing the dynamic thermoelectric and thermomagnetic effects in-and-out of equilibrium, the first part of our work focused on documenting the mathematical approaches to the problem, clarifications and refinements of the existing theories and models.

The general framework consisted in the study of a metallic rod subjected to a temperature gradient; the metal is of a type and geometry common in spacecraft missions, e.g., a cylindrical Au-Pt, Ti or Al rod with different cross-sections. The end result is a complex model obtained by integrating the information about parameter space, the skeleton models and proposed refinements.

The next step was to simulate configurations as close as possible to those of SWARM; as a consequence, the main part of our work focused on defining SWARM fiducial configurations, implementing them into COMSOL[3] and presenting the results of numerical simulations.

The end goal was to aggregate the information produced by theory and simulations and to put it in a mission oriented context. Detailed analysis of the simulations was presented, in order to produce a theoretical and quantitative description of the results. An overview of the resulting magnetic field was discussed for the fiducial configurations and for other geometries. Based on these results, an algorithm to solve the disturbance issue at the data processing level and magnetic cleanliness methods are proposed.

[3]COMSOL is the simulation tool we have used to produce the contracted numerical results. For details on this simulation tool please visit `https://www.comsol.com`

Chapter 2

Work and findings

2.1 Theory and refinements

The thermomagnetic theory of solids is a well established branch of physics [5, 7, 8, 9, 10, 11]. Starting from basic nonequilibrium thermodynamic principles, one can formulate evolution laws for the electric and thermal flows appearing in a metal rod subjected to both electric and thermal gradients. The equations describing these flows contain coefficients whose numerical values set the importance of each of the terms. As such, the smaller the coefficient, the less important the contribution of its associated term. Table 2.1 contains numerical estimates for the coefficients in space conditions.

Symbol and name	**Comments (numerical values in SI)**
σ, electrical conductivity	See Table 2.3, column 3
κ, thermal conductivity	At room temperature, the most heat conductive of the materials from Table 2.3 is copper, with $\kappa = 401$, and the least heat conductive is CFRP, with $\kappa \in (0, 10)$
α_S, Seebeck coefficient	For metals and metallic alloys, $\alpha_s \in (-10, 10)$, but for most cases $\alpha_S \in (-3, 3)$. For example, for copper, $\alpha_S \sim -10^{-5}$
π, Peltier coefficient	$\pi = T\alpha_S$, with $T = 300K$
τ, Thomson coefficient	$\tau = T\frac{d\alpha_S}{dT}$
ϵ, absolute thermoelectric power	$\equiv \alpha_S$
σ_i, σ_a isothermal and adiabatic electrical conductivities	Conductivities measured in isothermal conditions vs. measured in adiabatic conditions differ mainly in 1) the contribution of the phonon gas (whose behavior is determined by thermal energy) and 2) the contribution of the electron gas (whose behavior is determined by all electric, thermal and magnetic conditions); $\sigma_a/\sigma_i = 1 + \sigma_a T\epsilon^3/\kappa_i$; $\approx \sigma$
κ_i, κ_a isothermal and adiabatic thermal conductivity	For $\nabla T = 0$, $\kappa_a = \kappa_i \approx \kappa$; If $\nabla T \neq 0$, $\kappa_a/\kappa_i = 1$+small quantity;
E, Ettinghausen coefficient	$T\eta_i/\kappa_i$, $E \sim 10^{-4}$
$\mathcal{L}$, Leduc-Righi coefficient	close to 1
R_i, isothermal Hall resistance	for cubic lattice metals, $R_i \approx -1 \times 10^{-11}$
R_a, adiabatic Hall resistance	$\approx R_i$ when lattice contributions to heat transfer are dominant; in general $R_a/R_i = 1 + T\epsilon\eta_i/(R_i\kappa_i)$
η_a, adiabatic Nernst coefficient η_i, isothermal Nernst coefficient	in general, $\eta_a/\eta_i = 1 - \epsilon\mathcal{L}/\eta_i$; straightforward calculations show that for $R_a \sim 10^{-11}$, $\epsilon \sim 1$ and $\sigma \sim 10^7$, $\eta_{a,i}$ is $\sim 10^{-4}$

Table 2.1: Estimate numerical values for the thermoelectric and thermomagnetic coefficients in space conditions

The parameters external to the material are discussed in Table 2.2.

Symbol	Name	Value	Comments
T_{ext}	External temperature	Within $\pm 10^2$ $°C$	General order of magnitude of interest; much lower than the Fermi temperature of the materials of interest
		300K	Tested in [6], laboratory
		$-100/100\,°C$	Temperature in Low Earth Orbit (LEO) [13]
		$-50/50$ $°C$	Recorded on SWARM [12]
∇T	Applied temperature gradient	$20K/m$	Tested in [2], laboratory
		1 $°C/cm$	Tested in [6], laboratory
		25 $°C$	Temperature swing on SWARM [3]
		–	Standard SWARM data [12] does not contain gradient information. We have requested information about the temperature on the ASM to calculate T_{VFM}–T_{ASM} and obtained that $\nabla T \sim 10 - 15K$
B_{ext}	External magnetic field	$5 \cdot 10^{-5}$ T	Terrestrial magnetic field in Paris [13]
		10^{-6} T	Terrestrial magnetic field anticipated in LEO [13]
		10^{-5} T	Order of magnitude measured by SWARM onboard detectors [12]

Table 2.2: Parameters external to the material

The parameters characteristic to the material are summarized in Table 2.3.

Material parameters considered here (Table 2.3) do not necessarily provide an exhaustive description of all properties of the material, but they are nonetheless useful for a direct comparison of the materials with regard to the considered applicability. These parameters describe the following behaviours:

- Magnetic: the magnetic susceptibility χ describes the ability and modality to react under an applied magnetic field. This may not cause the new thermomagnetic effect, but may influence quantitative results.
- Electrical: since our concern is in the new thermomagnetic effect, we consider the electrons that, by moving within the metal, produce the current causing the magnetic field; of interest are mainly the electrons that start moving due to the temperature gradient. The number of activated electrons at a given temperature T depends on the Fermi temperature of the material, $T_F = E_F/k_B$ (where T_F is the Fermi energy).
- Electrical: the main scattering mechanism of the moving electrons is by interaction with phonons; the scattering mechanisms are included in the electrical conductivity σ.

The parameters characteristic to the problem are shown in Table 2.4.

Material (symbol)	**Fermi temperature T_F [K]**	**Electrical conductivity σ $[S/m]$, at $20°C$**	**Magnetic susceptibility χ [dimensionless] at $20°C$**	**Comments**
Aluminum (Al)	$13.40 \cdot 10^4$	$3.50 \cdot 10^7$	$2.20 \cdot 10^{-5}$	
Titanium (Ti)	$12.90 \cdot 10^4$	$1.80 \cdot 10^6$	$19.63 \cdot 10^{-5}$	
Copper (Cu)	$8.10 \cdot 10^4$	$5.98 \cdot 10^7$	$-0.71 \cdot 10^{-5}$	
Silver (Ag)	$6.38 \cdot 10^4$	$6.30 \cdot 10^7$	$-2.60 \cdot 10^{-5}$	
Gold (Au)	$6.42 \cdot 10^4$	$4.52 \cdot 10^7$	$-3.64 \cdot 10^{-5}$	
Brass	$0(10)^4$	$\mathcal{O}(10)^6$	< 0	Diamagnetic at 20 $°C$
Aluminum alloy AL AU4G (2017 A T3)	$\mathcal{O}(10)^4$	$\mathcal{O}(10)^7$	$\mathcal{O}(10)^{-5}$	T_F of metal alloys cannot be lower than the lowest of the metals in the alloy.
Ti alloy Ti grade V (TA6-V)	$\mathcal{O}(10)^4$	$5 \cdot 10^5$	$\mathcal{O}(10)^{-6}$	T_F of metal alloys cannot be lower than the lowest of the metals in the alloy.
Stainless steel (austenitic)	$\mathcal{O}(10)^4$	$\mathcal{O}(10)^6$	$\mathcal{O}(10)^{-2}$	T_F of metal alloys cannot be lower than the lowest of the metals in the alloy. χ is given for fully annealed austenitic stainless steel. Values differ in a large interval for different types of stainless steel.
Compound Au (75%) – Pt (25%)	$\mathcal{O}(10)^4$	$\mathcal{O}(10)^7$	-	T_F of metal alloys cannot be lower than the lowest of the metals in the alloy. No data on χ could be found.
CFRP M55J EX1515	-	$\mathcal{O}(10)^4$	-	No data on T_F and χ could be found.

Table 2.3: Parameters characteristic to the material

Symbol	**Name**	**Value**	**Comments**
$\lvert\delta B_{Sun}\rvert$	Scalar residual of in-flight magnetic field data	$963pT$	[3] Value of magnetic field disturbance caused by the Sun
-	Length	$1.5cm$	[6] Geometrical dimensions of the metal rod (cylindrical), experimental
-	Radius	$1.5cm$	

Table 2.4: Parameters characteristic to the problem

Our calculations show that the formula given as end result in [6] is inappropriate. We present here the final result of our calculations:

Our results	Results in [6]
$\vec{j} = -\frac{\pi^2 \sigma k_B}{3eT_F} T \nabla T$	Their eq. (26) $\vec{j} = \sigma T \frac{T_D^3}{T_F^2} \frac{k_B}{e} \frac{\nabla T}{T^2}$

To calculate the magnetic field produced by a current loop we thus use the current density

$$\vec{j} = -\frac{\pi^2}{3e} k_B \sigma \frac{T}{T_F} \nabla T, \tag{2.1}$$

where T is the ambient temperature, T_F is the Fermi temperature of the material and ∇T is the temperature gradient along the cylinder.

Assuming that the temperature gradient $|\nabla T|$ and the cross-section area A are constant with respect to spatial coordinates, the expression for the total magnetic field at $\vec{r}_0$ is, according to the Biot-Savart law:

$$\vec{B}(\vec{r}_0) = \frac{\mu_0}{4\pi} A\alpha |\nabla T| \sum_i \int_i \frac{d\vec{l}_i \times \vec{r}_i}{r_i^3}. \tag{2.2}$$

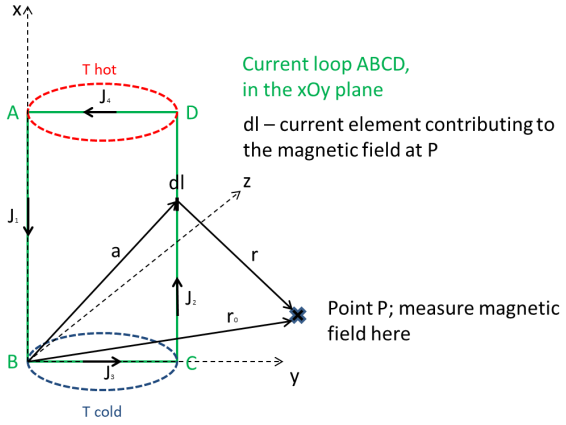

Figure 2.1: Graphical representation of the simplified configuration used to calculate the magnetic field at a point P.

Let us denote the integral by $\vec{G}$,

$$\vec{G}(\vec{r}_0) = \sum_i \int_i \frac{d\vec{l}_i \times \vec{r}_i}{r_i^3},$$

and write it explicitly for a rectangular current loop ABCD, with corners with coordinates $A(L, 0, 0)$, $B(0, 0, 0)$, $C(0, 2R, 0)$, $D(L, 2R, 0)$ (Figure 2.1) as

$$\vec{G}(\vec{r}_0) = \int_0^L \frac{(x, 0, 0) \times (\vec{r}_0 - (x, 0, 0))}{(\vec{r}_0 - (x, 0, 0))^3} dx + \int_0^L \frac{(-x, 0, 0) \times (\vec{r}_0 - (x, 2R, 0))}{(\vec{r}_0 - (x, 2R, 0))^3} dx$$

$$+\int_0^{2R}\frac{(0,-y,0)\times(\vec{r}_0-(0,y,0))}{(\vec{r}_0-(0,y,0))^3}dy+\int_0^{2R}\frac{(0,y,0)\times(\vec{r}_0-(L,y,0))}{(\vec{r}_0-(L,y,0))^3}dy.$$

This integral may be easily calculated with dedicated software, such as Mathematica, Octave, Matlab, Maple.

2.2 Numerical simulations

The analytical approach can only go so far when it comes to accounting for the complexity of the real situation. The next step is to build a simulation to obtain numerical results.

Two fiducial configurations were set: SWARM1 (Figure 2.2, to model the Absolute Scalar Magnetometer (ASM) configuration) and SWARM2 (Figure 2.3, to model the Vector Field Magnetometer (VFM) configuration).

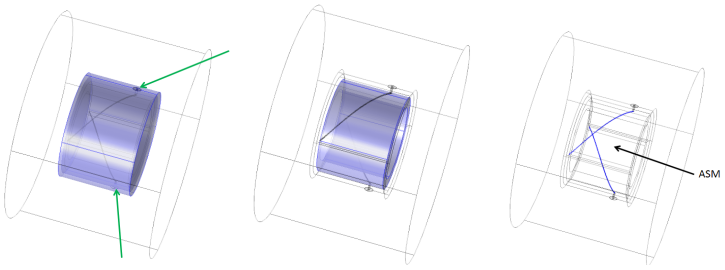

Figure 2.2: SWARM1-2 geometry in COMSOL (ASM). Left: The two Al rivets are placed symmetrically with respect to the axis of the cylinder; marked in blue is the MLI (Multi-Layer Insulation). Middle: The Cu wires are displayed along a long route, in order to simulate a current loop around the ASM; marked in blue is the CFRP. Right: ASM placement with respect to the wires.

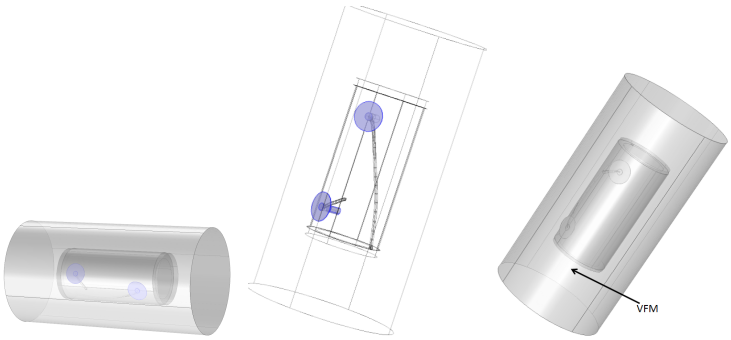

Figure 2.3: SWARM2 geometry in COMSOL (VFM, rivets oversized for better visualization). Left: The two Al rivets are placed on the same side with respect to the axis of the cylinder. Middle: Cu wires and rivets are displayed. Right: VFM placement with respect to the wires.

The materials used on SWARM and their arrangement are complicated. To obtain qualitative and fairly useful quantitative results about the generation of thermoelectric fields in such cases, the complexity of the real configuration is greatly reduced in the numerical approach. The configuration we considered is based on a simplified description of the SWARM magnetometer placement: inside a hollow or near a Carbon Fiber Reinforced Polymer (CFRP) cylinder, which is covered with a metallic

blanket (MLI). On this blanket, two aluminum rivets are used to clamp the blanket; the rivets are grounded by copper wires.

As a consequence, the following physical entities exist in the simulations:

(E_1) plastic tube (CFRP), full or hollow (with air in it)

(E_2) air between tube and blanket

(E_3) metallic blanket (MLI); this needs to wrap completely around the tube, at all ends and margins

(E_4) two Cu wires, located in the air between tube and blanket

(E_5) the surrounding air

(E_6) two Al rivets, one at T_{hot} and one at T_{cold}, clamping the blanket, and as such going through/belonging to the following media: air outside (E_5), MLI (E_3), air between tube and blanket (E_2)

The two configurations, SWARM1 and SWARM2, differ in respect to:

- placement of Al rivets
  - SWARM1: placed symmetrically with respect to the cylinder axis, at the same height
  - SWARM2: placed roughly on the same generator of the cylinder
- configuration of Cu wires
  - for SWARM1, two configurations are used: SWARM1-1, where the Cu wires are allowed to follow the shortest route to the satellite casing, and SWARM1-2, where the Cu wires follow a longer route, such as to model a current loop around the cylinder
  - for SWARM2 we used a long wires configurations
- condition of the CFRP tube: hollow (or nonexistent) in SWARM1 and full in SWARM2

The characteristics of each entity in the simulations are:

(E_1) plastic tube (CFRP), a cylinder of radius R and length L, $\mathcal{C}(R, L)$: for each of the two configurations we chose as representative the imaginary cylinder circumscribed about each of the two constructions: ASM and VFM [14],[15].

(E_2) air between tube and blanket: from configuration assembly it is clear that the MLI is not airtight to the tube, i.e., the air width is at least as thick as a Cu wire.

(E_3) metallic blanket (MLI): as per [16], the MLI used on SWARM is EXT-BTVA-K, having multiple layers with a calculated total thickness of at least ≈ 0.002 m (without the Ti sewing). The MLI will be simulated by a single metallic layer (instead of all the different layers contained in the MLI), with properties equivalent to those of the entire MLI. The choice of material properties is based on the fact that the two outermost layers of the MLI are the titanium sewing and the vapor-deposited aluminum: we used the Seebeck coefficient α_S of titanium, but allowed this parameter to be public, so it would accommodate any new information that might arise about material properties.

(E_4) Cu wires, modeled as a helix of thickness w_{Cu}, l_{Cu} and N_{Cu} turns.

(E_5) the surrounding air: the simulator is able to propagate solutions as far out around the satellite as needed, but in this case it will not be necessary. We will consider the surrounding air (geometrically defined as a larger cylinder in which the cylindrical layer of metal is immersed) to have the dimensions $\mathcal{C}(2R, 2L)$.

(E_6) Al rivets: are modeled as a top cylinder $\mathcal{C}(R_{r1}, L_{r1})$ with a large radius-to-height ratio and a slender cylinder $\mathcal{C}(R_{r2}, L_{r2})$. The dimensions were chosen after consulting [17].

An overview of parameters in the simulations is given in Table 2.5. The identifier "private" or "public" refers to how the end user of the simulation application interacts with the parameter: if it is "public", the end user will be able to modify it and recompile the simulation so as to obtain new results.

Geometry	Identifier	Value, in [IS]
Radius of CFRP cylindrical layer (SWARM1)	public	$R = 0.17$
Height of CFRP cylindrical layer (SWARM1)	public	$L = 0.315$
Width of CFRP layer (SWARM1)	public	$w_1 = 0.02$
Radius of CFRP cylinder (SWARM2)	public	$R = 0.04$
Height of CFRP cylinder (SWARM2)	public	$L = 0.2$
Width of MLI	private	$w_m = 0.005$
Width of air between MLI and CFRP	private	$w_a = 0.005$
Radius of Al rivet - top	private	$R_{r1} = 0.004$
Height of Al rivet - top	private	$L_{r1} = 0.001$
Radius of Al rivet - body	private	$R_{r2} = 0.001$
Height of Al rivet - body	private	$L_{r2} = 0.01$
Thickness of Cu wire	private	$w_{Cu} = 0.001$
Length of Cu wire	private	$l_{Cu} = 0.2$
Number of turns of Cu helix	private	$N_{Cu} = 0.25$
Properties		
metallic blanket Seebeck coefficient	public	$\alpha_S = -5 \cdot 10^{-5}$
metallic blanket electric permittivity	private	1
metallic blanket magnetic permeability	private	1
metallic blanket electric conductivity	public	$5 \cdot 10^5$
metallic blanket thermal conductivity	private	16.4
metallic blanket heat capacity	private	523
metallic blanket density	private	4500
Air Seebeck coefficient	private	0
Air electric permittivity	private	1
Air magnetic permeability	private	1
Cu wires Seebeck coefficient	private	$1.9 \cdot 10^{-6}$
Cu wires electric permittivity	private	1
Cu wires magnetic permeability	private	1
Al rivets Seebeck coefficient	private	$-1.8 \cdot 10^{-6}$
Al rivets electric permittivity	private	1
Al rivets magnetic permeability	private	1
Al rivets heat capacity	private	904
CFRP Seebeck coefficient	private	0
CFRP electric permittivity	private	3
CFRP electric conductivity	private	0
CFRP magnetic permeability	private	1
CFRP thermal conductivity	private	155
CFRP heat capacity	private	711
CFRP density	private	7550
Parameters		

Temperature of air around the configuration and of the cold rivet on the cylinder	private	$T = 300$
Temperature gradient	public	$\nabla T = 15$

Table 2.5: Input parameters in the simulations

2.3 Assessment of main contributors

The metal parts involved in generating the new thermomagnetic effect are:

M_1 : metallic blanket,

M_2 : Cu wires,

M_3 : Al rivets, where the hot rivet is denoted by R_h and the cold rivet by R_c.

All metal parts were removed from the configurations, both one at a time and in all possible combinations, and the magnetic field was calculated in relevant points (the estimated position of the ASM and VFM magnetometers) (see results in Table 2.6).

Configuration	$\lvert\vec{B}\rvert$	B_x	B_y	B_z
SWARM1-1	20.17	$-9.55 \cdot 10^{-2}$	-20.17	0.215
SWARM1-1 without M_1	$1.27 \cdot 10^{-3}$	$9.79 \cdot 10^{-5}$	$-1.27 \cdot 10^{-3}$	$-1.72 \cdot 10^{-5}$
SWARM1-1 without M_2	23.95	3.4	23.53	2.86
SWARM1-1 without M_3	57.11	53.22	18.18	9.92
SWARM1-1 without M_1, M_2	$1.98 \cdot 10^{-3}$	$-2.33 \cdot 10^{-5}$	$-1.98 \cdot 10^{-3}$	$6.05 \cdot 10^{-5}$
SWARM1-1 without M_2, M_3	20.2	1.24	20.11	-1.41
SWARM1-1 without M_1, M_3	$1.57 \cdot 10^{-4}$	$1.10 \cdot 10^{-5}$	$-1.56 \cdot 10^{-4}$	$-2.81 \cdot 10^{-6}$
SWARM1-2	40.46	-36.44	-8.28	15.49
SWARM1-2 without M_1	4.53	3.15	-1.11	3.07
SWARM1-2 without M_2	23.95	3.4	23.53	2.86
SWARM1-2 without M_3	49.70	47.63	11.34	8.55
SWARM1-2 without M_1, M_2	$1.98 \cdot 10^{-3}$	$-2.33 \cdot 10^{-5}$	$-1.98 \cdot 10^{-3}$	$6.05 \cdot 10^{-5}$
SWARM1-2 without M_2, M_3	20.2	1.24	20.11	-1.41
SWARM1-2 without M_1, M_3	4.47	3.04	-1.22	3.03
SWARM2	133.42	-92.85	93.91	-18.97
SWARM2 without M_1	2	1.96	0.25	0.31
SWARM2 without M_2	134.59	-79.42	108.65	$7.33 \cdot 10^{-2}$
SWARM2 without M_3	205.6	-132.43	156.88	-10.98
SWARM2 without M_1, M_2	$1.42 \cdot 10^{-3}$	$-6.91 \cdot 10^{-3}$	$-1.24 \cdot 10^{-3}$	$3.39 \cdot 10^{-5}$
SWARM2 without M_2, M_3	237.47	-131.11	197.42	-15
SWARM2 without M_1, M_3	2.36	2.31	0.35	0.34

Table 2.6: Comsol-calculated values of the magnetic field disturbance (in nT) in SWARM fiducial configurations: assessment of individual contributors

Table 2.6 shows that the most important contributor to the magnetic field is the metallic blanket

for SWARM1-1 (short Cu wire configuration) and the combination between blanket and wires for SWARM1-2 and SWARM2 (both with longer Cu wires configurations).

The tested configurations are complex and have no symmetries (due to the geometrical arrangement of wires and rivets). A series of analyzes were conducted, for SWARM1-1, SWARM1-2 and SWARM2 full configurations:

A_1 a set of representative point probes were defined,

A_2 analysis of the thermal behavior of the configuration,

A_3 analysis of the current density vector,

A_4 analysis of the impact of the length of the copper wires,

A_5 analysis of the impact of the width of the metallic layer.

Tables 2.7-2.9 contain the conclusions of running analyzes A_1-A_5 for the three fiducial cases.

Analysis	Conclusion/ Comments
A_1	A total of 6 probe points were defined, 2 on the symmetry axis (estimate position of ASM) and 4 on the circle centered in the ASM, with a $R_{tube}/2$ radius (the plane of this circle is orthogonal to the symmetry axis). As expected, the magnetic field is stronger in the point closer to the rivets. On the circle, however, there is an order of magnitude variation of the values in the 4 points: lower on the cold rivet side and higher on the hot rivet side. It appears that, even though the configuration is geometrically symmetric, the temperature gradient introduces an asymmetry in the electron flow and thus the disturbance magnetic field will be asymmetric.
A_2	As expected, the heat flows from the heated rivets towards the surrounding media. Since electrons start flowing from the cold rivet along the blanket (as explained below), there will also be a smaller heat flux originating from the colder rivet.
A_3	The electric flow has two components of different magnitude: a larger one from the rivets towards the blanket and a smaller one, from R_c isotropically to the blanket and towards R_h isotropically from the blanket. The phenomenon can be explained as follows: in the hot rivet, electrons will start to flow from the rivet, through the wire, towards the grounding. An electric potential is set up between this rivet and the cold one; thus electrons from the cold rivet will flow along the blanket towards the hot rivet. The picture is very clear because in this configuration the Cu wires are extremely short.
A_5	Identical simulations were run, changing only the thickness of the metallic blanket; an attempted fit would be a linear one: $B[nT] = 9 + 1790.81w$ (w in m), although the spread around the fit is quite large. However, no better fit is provided by higher degree polynomials, exponential or harmonic functions.

Table 2.7: Results of A_1-A_5 for SWARM1-1 (the A_4 analysis was not performed on SWARM1-1).

Analysis	Conclusion/ Comments
A_1	A total of 6 probe points were defined, 2 on the symmetry axis (estimated position of ASM) and 4 on the circle of radius $R_{tube}/2$ centered on the ASM position (the plane of this circle is orthogonal to the symmetry axis). As expected, the magnetic field is larger in the point closer to the rivets. On the circle, however, there is an order of magnitude variation of the values in the 4 points: lower on the cold rivet side and larger on the hot rivet side.
A_3	The electric current shows two components in term of magnitude: the larger one flows along the wires, from the rivets to the grounding; a second component, of smaller magnitude, is directed from the cold rivet, along the blanket, to the hot rivet. The reasons for this were explained in Table 2.7.
A_4	Simulations were performed for SWARM1-2 without M1 and M3 (metallic blanket and rivets, respectively). In this case, it is just the wire at T_{hot} that produces a magnetic field, since the other one is at ambient temperature.
A_2, A_5	Aside from introducing a new source of electrons, the blanket also ensures thermal coupling between the two wires (the ambient air is always kept at constant temperature, meaning that, in the absence of the blanket, the two Cu wires are not thermally coupled). The collaborative effect is not a linear combination of the individual metallic parts. The analytic dependency between the disturbance magnetic field and the width of the metallic layer is a second degree polynomial $B[nT] = 9.45597 + 5787.09w + 596210w^2$, with w in meters.

Table 2.8: Results of A_1-A_5 for SWARM1-2

Analysis	Conclusion/ Comments
A_1	A total of 6 probe points were defined, 2 on the symmetry axis (estimated position of VFM) and 4 on the circle of radius $R_{air}/2$ centered on the position of the VFM (the plane of this circle is orthogonal to the symmetry axis). As expected, in the point closer to the cylinder the magnetic field is almost double. On the circle, however, the values vary in the 4 points by almost an order of magnitude. One major contributor to the problem is thus the lack of symmetry with respect to the axis of the cylinder (which is of interest because the VFM is positioned here) caused by the rivets and the wires.
A_2	The heat flux has 2 distinctive components: most of the heat flux runs along the Cu wires, with the electron flow. Since the blanket itself gets warmer, there will be a smaller heat flux perpendicular to the metallic blanket.
A_3	The current density has 2 distinctive components: the larger one runs along the copper wires; the smaller value component is directed along the blanket.
A_4	Changing the copper wire length in this particular configuration does not have a significant effect (it does not change the order of magnitude of results). The analytic dependency found after fitting simulated data is that the disturbance magnetic field behaves as a third order polynomial with respect to the Cu wire length $B[nT] = 4.31 + 1019.77L - 2396.37L^2 + 1737.38L^3$, with L in meters.
A_5	The behavior of the disturbance magnetic field is nonlinear with respect to the width of the metallic blanket. The best fitting function is a second degree polynomial $B[nT] = -42.26 + 47848.7w - 2.75 \cdot 10^6 w^2$, with w in meters.

Table 2.9: Results of A_1-A_5 for SWARM2

SWARM1-1 shows three magnetic fields of different magnitudes: a larger one in the vicinity of the hot rivet, a smaller one in the vicinity of the cold rivet and the smallest over the rest of the configuration (Figure 2.4 left[1]). The magnetic field around the rivets is oriented mainly in the zy plane, i.e., it has a strong component parallel to the cylinder axis. Over the rest of the configuration, including the area where the ASM is located, the magnetic field has a very weak, if not zero, component along the z axis. In conclusion, at the ASM position, the z component of the disturbance magnetic field is close to zero (negligible by comparison to the other components). These results are corroborated by plots of the magnitude of the magnetic field at the ASM position.

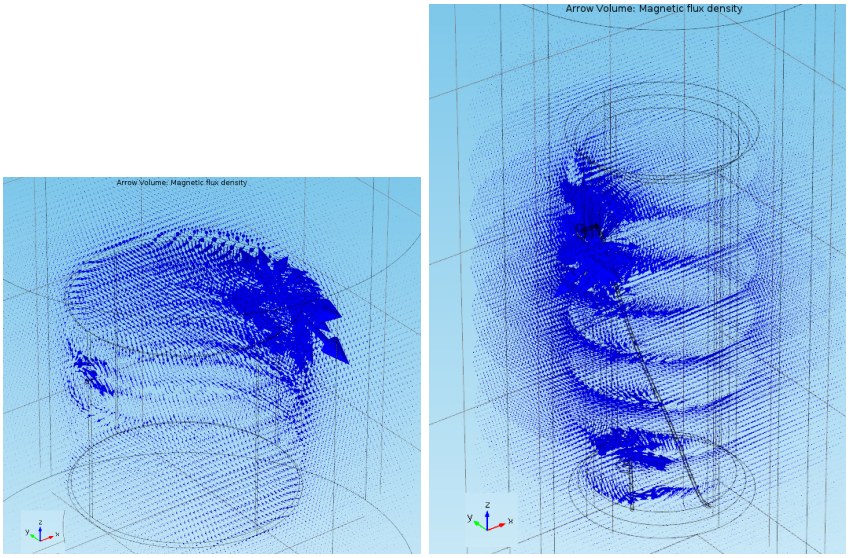

Figure 2.4: Magnetic field vector, left: SWARM1-1, right: SWARM2

The same conclusions are valid for **SWARM1-2**.

For the **SWARM2** configuration, again three categories of magnetic field can be identified, with respect to their magnitude. The largest magnitude is found in the vicinity of the hot rivet, parallel to the yz plane; the second largest magnetic field appears around the cold rivet, also in the yz plane. The rest of the configuration is permeated by a low intensity magnetic field, perpendicular to the cylinder axis (Figures 2.4 right). Since the VFM is located outside the metallic blanket, approximately along the axis, the conclusion is that the z component at this position should be negligible as compared to the xy components.

2.4 Algorithm to solve the issue at data processing level

The question arises whether or not the magnetic field disturbance problem can be solved at data processing level. The answer is "yes, but..."

We generally believe this problem can be solved by way of software and below we will offer a general algorithm on how it can be done; the actual platform can be established by the team that takes on this task. However, in the particular case of SWARM (already on orbit), since the assembly configuration is not fully documented, the approach discussed throughout the project cannot offer a better alternative than the numerical methods already developed by the SWARM engineers. The proposed algorithm needs precise measurements and localization regarding the copper wires. The conditions that would allow the issue to be solved at data processing level in the future are as follows:

[1]Please note that the notation of the axes in Figure 2.4 is different with respect to the one in Figure 2.1.

1. input data to the simulator (e.g., the length and spatial arrangement of the copper wires and the rivets) must be unambiguous;

2. a full analytical/functional/physical description of the MLI must be provided; the geometrical description exists, but the MLI is a complex system of materials. If its entire contribution to the magnetic field disturbance is to be considered, a full description of the MLI must be included in the simulator, especially its overall material properties;

3. individually tested and documented material properties, especially of the thermoelectric properties of all materials used; unambiguous and self-consistent conceptual definition and measurement of Seebeck coefficients;

4. the grounding potential for the copper wires needs to be known with precision.

If the simulator is set up to offer a one-to-one correspondence to the real-life satellite arrangement, the simulation output may be used to correct the magnetic field measurements at data processing level (Figure 2.5). The simulation output consists in the magnetic field value on a three-dimensional spatial grid, where the mesh may be as fine as desired. This value may then be subtracted from the measured magnetic field and the result would be the "real" magnetic field.

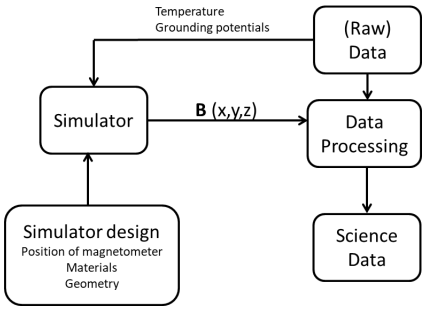

Figure 2.5: Proposal for a general algorithm to correct magnetic field data at data processing level

2.5 Magnetic cleanliness methods

The end value of the disturbance magnetic field is the result of a collaborative effect between the metallic parts in the configuration. Our discussion so far has shown that the spatial arrangement of the disturbance magnetic field is in the plane parallel to the rivet in the vicinity of the rivets and in the plane perpendicular to the symmetry axis of the cylinder in the rest of the configuration. Equipped with this information, the magnetometer may be placed accordingly. Also, in the future, the positioning of the rivets can be changed, which would alter the spatial arrangement of the resulting disturbance magnetic field.

Material properties are extremely important in the appearance of the disturbance magnetic field. We have conducted simulations where the Seebeck coefficient of the metallic blanket is positive (i.e., contrary to fiducial). SWARM1-2 was used as a base structure. The results differ only slightly: the magnitude of the magnetic field is almost the same, but, since the current is traveling in opposite direction, the magnetic field changes orientation with almost 180°. Thus, changing the sign of the Seebeck coefficient of the blanket flips the orientation of the magnetic field by 180°.

We have conducted simulations with a negative Seebeck coefficient for the conducting wires (i.e., contrary to the fiducial case). SWARM1-2 was used as base structure. The magnetic field (including its orientation) measured at the ASM location is almost the same as for the fiducial case.

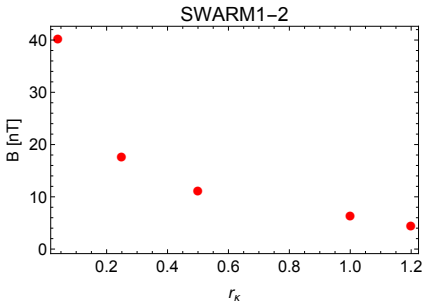

Figure 2.6: SWARM1-2: dependency of the disturbance magnetic field at the ASM location with respect to the Seebeck coefficient (left) and the ratio r_κ (right)

To investigate the importance of the magnitude of the Seebeck coefficient of the blanket (retaining its sign with respect to the fiducial configuration) we performed simulations based on SWARM1-2. The behavior of the resulting magnetic field disturbance at the ASM location is shown in Figure 2.6 left and is very well fitted by a first degree polynomial function, $B[nT] = 4.36 - 0.72\alpha_S[\mu V/K]$.

Further, using again SWARM1-2 as starting point, simulations were ran to test the effect of the ratio of thermal conductivities, $r_\kappa = \kappa_{M_1}/\kappa_{M_2}$. In the fiducial configurations, $r_\kappa = 0.0405$; with κ_{M_2} kept constant, the thermal conductivity of the blanket was varied such as to increase r_κ. For $r_\kappa = 0.25$ the value of the magnetic field at the ASM location drops to more than half with respect to fiducial. The general behavior of the magnetic field with respect to r_κ is shown in Figure 2.6 right.

As a conclusion to all the trends we have documented regarding the dependencies of the disturbance magnetic field, we ran a simulation based on the SWARM1-2 configuration, with $w = 0.001m$, $\alpha_S = 10^{-6}V/K$ for the blanket and $r_\kappa = 1.5$. The results, $|\vec{B}| = 2.02$, $B_x = -1.86$, $B_y = 0.64$ and $B_z = 0.42$, show that **the magnitude of the magnetic field decreased 20 times with respect to the fiducial configuration and its z component has dropped by two orders of magnitude.**

Chapter 3

Conclusions

The achievements of this work fall in two broad categories: theoretical and numerical. For the theoretical part we have shown that the formula used thus far for estimating magnetic field disturbances is not appropriate. We have derived appropriate formulas for the electric current density and resulting vector magnetic field disturbance.

The numerical part consists of a numerical simulator for a complex configuration of cylindrical layers of different materials, with 2 rivets clamping the outer layer and 2 wires grounding the configuration (to the ship). The material properties and dimensions of the geometry are public variables. This means that the full set of numerical results may be re-obtained for different values of the public variables. As a consequence, the end user need not be familiar with the numerical tool used; i.e., the code is provided both source and object code.

For all studied configurations, the magnetic field is essentially two-dimensional in any point at some distance from the rivets (i.e. at the currently assumed positions of the magnetometers). The magnitude of the magnetic field depends linearly or quadratically on the width of the metallic layer.

The achievements also include suggestions on how to decrease the order of magnitude of the disturbance magnetic field and a schematic of a feedback loop to correct for the disturbance at the data processing level.

Bibliography

[1] Statement of Work, Magnetic Field Perturbations by Thermoelectric Effects, ESA-TECEEE-SOW-003094

[2] Jager, T. Leger, J.M., Fratter, I., Lier, P., Pacholczyk, P., Magnetic Cleanliness and Thermomagnetic Effect: Case study of the absolute scalar magnetometer and its environments on SWARM satellites, in: Proc. 2016 ESA Workshop on Aerospace EMC, Valencia, Spain, May 23-25, 2016, ESA-SP-738

[3] Toffner-Clausen, L. et al., In flight scalar calibration and characterization of the SWARM magnetometry package, in: Earth, Planets and Space (2016), 68:129

[4] ESA Contract 4000122501 with the Romanian Academy

[5] Callen, H., Thermodynamics. An introduction to the physical theories of equilibrium thermostatics and irreversible thermodynamics, Wiley (1962)

[6] Vasiliev, B.V., The new thermomagnetic effect in metals, Universal Journal of Physics and Application (2014), 2:4, pp. 221-225

[7] Rowe, D.M. (ed.), Thermoelectrics Handbook: Macro to Nano, CRC Taylor and Francis, 2006

[8] Kittel, C., Introduction to Solid State Physics, 5th Edition, Wiley & Sons, 1976

[9] Kittel, C., Thermal Physics, Wiley & Sons, 1976

[10] Chien C.L and Westgate C.R. Eds, The Hall effect and its applications, Springer Science + Business Media, LLC, 1980

[11] Ashcroft, M., Mermin, N., Solid State Physics, Thomson Learning, 1976

[12] SWARM data - Courtesy of ESA

[13] `https://directory.eoportal.org/web/eoportal/satellite-missions/s/swarm`

[14] SWARM Carbon Tube Assembly, Interface Control Document, SW-IF-RAW-SC-0001, courtesy of RUAG

[15] SWARM Optical Bench, Interface Control Document, SW.ID.EAD.OA.00014, courtesy of RUAG

[16] SWARM MLI detailed design description, courtesy of RUAG

[17] SWARM S/C MLI Declared Material List, DML/DMPL/DPL, SW-LI-AAE-SC-2005, courtesy of RUAG